

The Crossings of Saturn Ring Plane by the Earth in 1995: Ring Thickness

François Poulet

Département de recherche spatiale, Observatoire de Meudon, 92195 Meudon Cédex Principal, France

E-mail: francois.poulet@obspm.fr

Bruno Sicardy

Département de recherche spatiale, Observatoire de Meudon/Institut Universitaire de France, 92195 Meudon Cédex Principal, France

Christophe Dumas

Jet Propulsion Laboratory, Pasadena, California 91109

Laurent Jorda

Max-Planck-Institute Für Aeronomie, D-37191 Katlenburg-Lindau, Germany

and

Didier Tiphène

Département de recherche spatiale, Observatoire de Meudon, 92195 Meudon Cédex Principal, France

Received July 21, 1998; revised July 26, 1999

The crossings of Saturn's ring plane by Earth were observed in the near infrared on May 22 and August 10, 1995, from the 2.2-m telescope of the University of Hawaii, the 2-m telescope at Pic du Midi, France, and with the Adonis adaptive optics camera at the 3.6-m telescope of the European Southern Observatory in Chile. Images from the Hubble Space Telescope, obtained in August 1995, are also reanalyzed. The radial brightness profiles of the rings indicate that the outer and usually faint F ring dominates the edge-on brightness of the system, thus hiding the vertical structure of the main rings within a few hours around the ring plane crossing. The photometric behaviors of the A, B, and C rings and of the Cassini Division are analyzed, using a radiative transfer code which includes the illuminations by the Sun and by the planet. The F ring is modeled as a physically thick ribbon of height H , composed of large particles embedded in dust of fractional optical depth f . The observed profiles, combined with previous results, can be explained if the F ring is both optically thick (*radial* optical depth ~ 0.20) and physically thick ($H = 21 \pm 4$ km). We suggest that this vertical distribution results from the interactions between ring particles and shepherding satellites and/or from gravitational stirring by large bodies. The dust particles dominate the F ring's photometric behavior even in backscattered light ($f > 0.80$). Constraints on the particle properties of the other rings are also derived.

© 2000 Academic Press

Key Words: planetary rings, Saturn; photometry.

I. INTRODUCTION

The crossings of Saturn's ring plane by Earth and the Sun provide a unique opportunity to study the ring vertical structure. During the ring plane crossing (referred to as RPX hereafter) by Earth, the rings are viewed edge-on, thus yielding information about their global thickness. Previous groundbased observations of Earth RPXs, in December 1966 and in March 1980, provided estimates for the "equivalent photometric thickness" of 2.4 ± 1.3 km (Dollfus 1979) and $1.1_{-0.5}^{+0.9}$ km (Sicardy *et al.* 1982), respectively.

However, the various contributions entering in these numbers are still uncertain. Also, there is a conflict between the *global* photometric thickness of the rings and the internal velocity dispersion measurements, which yields a few tens of meters only for the *local* thickness (Esposito *et al.* 1983a). This discrepancy could stem from different effects: the 1.2-km full amplitude of the Mimas 5:3 bending wave (Shu *et al.* 1983, Lissauer 1985), consistent with the 1980 observations, and the 300-m warp of the Laplace plane due to torques from the Sun and Saturn's satellites (Burns *et al.* 1979). Other contributions to the edge-on ring brightness have been proposed, including the faint rings F, G, and E, the spokes observed in the Voyager images of the B ring, and even a tenuous dust halo resulting from the meteoroid–ring interactions (Ip 1995). A swarm of large ring particles of

1–2 km in radius could account for additional contributions to the edge-on brightness (Hénon 1982, Sicardy *et al.* 1982).

The most recent edge-on configurations occurred in 1995 and provided the last opportunity before the Cassini mission, starting in 2004. Earth crossed Saturn’s ring plane on May 22, 1995, around 6^{hr} UT, and again on August 10, 1995, around 21^{hr} UT; a third crossing took place on February 12, 1996, near 0^{hr} UT, but Saturn was then too close to solar conjunction for observations to be made properly.

The equivalent thickness of the rings derived from the May and August RPXs was similar to that found from the 1980 observations (Nicholson *et al.* 1996, Bosh *et al.* 1997). However, the high angular resolution of the 1995 observations, obtained through adaptive optics or the Hubble telescope, show that the radial profiles of the rings keep on increasing up to the radius of the F ring (~140,200 km), instead of dropping at the locations of the Mimas 5:3 bending wave or at outer edge of the A ring (136,780 km). Thus, it appears that the usually very faint F ring can play a dominant role in the observed profiles, at least within a few hours from Earth’s RPX. Therefore, a detailed photometric modeling of the various components of Saturn’s rings is in order to explain these profiles.

Besides the three Earth RPXs, a Sun RPX occurred on November 19, 1995, yielding a spectacular 2-D view of Saturn’s rings (Nicholson *et al.* 1996). Just outside the A ring, one can see the narrow F ring prominently visible, its brightness being comparable to that of the Cassini Division. If one assumes a flat F ring, the predicted brightness due to transmitted light cannot reproduce the observed brightness (Nicholson *et al.* 1996), indicating that the F ring cannot be considered as a classical narrow and flat ring. The arguments above are qualitative in nature, and it remains to be seen how the F ring could be thick and bright enough to explain the residual flux observed in the edge-on configuration.

In this paper, we collect several sets of observations obtained during the May and August 1995 Earth RPX’s. By analyzing and modeling the photometric profiles, we constrain the scattering properties of the particles of the main rings. We show that the photometric thickness of the rings is probably dominated by the F ring, whose physical thickness is estimated. Observations and data reductions are described in Section II. We then present the scattering model that we have used for the rings (Section III). The results are derived in Section IV and discussed in Section V.

II. PHOTOMETRIC DATA

II.1. Data and Image Geometry

The images analyzed here were essentially taken during the August 1995 Earth RPX, but we also have data obtained near the May 1995 Earth RPX. All these groundbased observations were made using near-infrared filters (K , K'), since the scattered light from Saturn is then greatly reduced by methane and molecular hydrogen absorptions. Images have been selected to encompass

the broadest possible distribution of sub-Earth latitudes on the ring plane near the RPX.

The geometry for the illumination of the rings by the Sun is defined by the three following angles:

- The subsolar latitude on the ring plane, B' . During the May RPX, B' was about 2.68° (with $\mu' \equiv \sin B' = 0.047$). In August, the Sun was more grazing, with $B' = 1.5^\circ$ ($\mu' = 0.026$).
- The sub-Earth latitude on the ring plane, B (with $\mu \equiv \sin B$). During the Earth RPX, the sign of B changes. So, we get two different configurations of the rings: the dark side is observed when B and B' have opposite signs, and the illuminated side become visible when these two angles have the same sign.
- The phase angle, α , defined as the Sun–rings–Earth angle. The angle α is about 5.55° in May and 3.55° in August.

In addition, we have to consider the illumination of the rings by the planet (i.e., the “Saturn shine”); see Section III.2.1 for details.

II.1.1. May 1995 Data Set

All the observations presented here were acquired with the 1024×1024 Quick Infrared Camera (QUIRC) at the 2.2-m telescope of the University of Hawaii (Mauna Kea). The scale is 0.1886 arcsec per pixel, resulting in a field of 193.1×193.1 arcsec². A standard broadband K filter centered at $2.2 \mu\text{m}$ was used. During the time span of the observations, Earth went from the northern (lit) side of the rings to the southern (dark) side. We analyzed images showing the dark side of the rings only, on May 22 and 23, 1995 (see Table I). The FWHM of the point spread function during the first night was between 6 and 8 pixels (~1.2–1.5 arcsec). The following night was worse with a typical seeing of 1.8 arcsec.

II.1.2. August 1995 Data Set

During the August RPX, groundbased observations at $\lambda = 2.15 \mu\text{m}$ were carried out with the Adonis (former Come-On+) adaptive optics system, mounted on the European Southern Observatory (ESO) 3.6-m telescope at La Silla, Chile (Table IIa). The conditions of observations are detailed in Poulet *et al.* (2000). Despite regular seeing conditions, the adaptive optics system reduces the FWHM of the point spread function to about 0.5 arcsec or less.

Figure 1 shows the east ansa of the rings, which provide an example of a profile taken a dozen hours before the Earth RPX. We observe a significant brightening due to the sunlight diffusely transmitted through the Cassini Division and the C ring. The radial profile of the dark side extends up to about 140,000 km from Saturn’s center, well outside of the outer edge of the A ring (136,780 km). This fact suggests a dominant contribution of the F ring and/or of a tenuous sheet of material between the F and A rings, at least at the outer parts of the profiles. The ESO data nearest to the RPX were taken ~11 h before the predicted RPX time (August 1995 at 10.875 ± 0.02 UT).

TABLE I
Hawaii Data (Dark Side)

Day	Exp ^a	Profile ^b	T ^c	Ansa ^d	B ^e	B' ^f	Calibration ^g
May 22, 1995	22.6104	H1	60	E	-0.0111	2.6734	Hyperion
	22.6180	H2	60	E	-0.0113	2.6733	Hyperion
	22.6215	H3	60	E	-0.0114	2.6732	Hyperion
May 23, 1995	23.5834	H4	60	E	-0.0399	2.6591	Hyperion
	23.5834	H5	60	W	-0.0399	2.6591	Hyperion
	23.5882	H6	60	E	-0.0401	2.6590	Hyperion
	23.5882	H7	60	W	-0.0401	2.6590	Hyperion
	23.6062	H8	120	E	-0.0406	2.6588	Hyperion
	23.6064	H9	120	E	-0.0406	2.6588	Hyperion
	23.6064	H10	120	W	-0.0406	2.6588	Hyperion

^a Decimal mid-exposure time in UT.

^b Name of profile.

^c Exposure time in sec.

^d Analysed ansa, E means east ansa and W west ansa.

^e Sub-Earth latitude on ring plane in deg.

^f Subsolar latitude on ring plane in deg.

^g Satellite used for photometric calibration (see Table III for the adopted magnitude).

Other groundbased data showing only the lit side were obtained with the 2-m telescope of the Pic du Midi observatory (Pic for short), using the infrared 256×256 "MOICAM" camera with a pixel size of 0.165 arcsec. Several sets of 15 frames were recorded in the standard *K* filters during the nights 11 and 12 August 1995 (Fig. 2). The seeing was roughly the same during the two nights, some images having a FWHM of 5 pixels (0.8 arcsec) on August 11. Table IIb lists the Pic data used here.

On August 10, 1995, the Wide Field and Planetary Camera 2 of the Hubble Space Telescope (HST) was targeted at Saturn

for an observing program (ID 5836) by Nicholson *et al.* (1996). A narrowband methane filter, centered at $0.89 \mu\text{m}$ was used for these images. Clear east-west asymmetries were noticed by Nicholson *et al.* (1996), the western ansa being $\sim 30\%$ brighter than the the eastern ansa 1 h or so after the RPX time. The data taking during this time (lit side) are only used to obtain approximate photometric properties of the main ring particles, which are then incorporated in the modeling of the dark side. So, images of the lit side showing strong asymmetries of brightness have been excluded from our analysis. The HST data used here are listed in Table IIc.

TABLE IIa
ESO Data (Dark Side)

Day	Exp	Profile	T	Ansa	B	B'	Calibration
August 9, 1995	9.2448	ESO1	60	W	-0.0458	1.5165	Enceladus
	9.2455	ESO2	60	W	-0.0458	1.5165	Enceladus
	9.2766	ESO3	60	W	-0.0449	1.5160	Janus
	9.2787	ESO4	60	W	-0.0448	1.5160	Janus
	9.4375	ESO5	60	E	-0.0403	1.5136	Tethys
August 10, 1995	10.3013	ESO6	60	E	-0.0158	1.5009	Janus
	10.3027	ESO7	60	E	-0.0158	1.5009	Janus
	10.3337	ESO8	60	W	-0.0149	1.5004	Tethys
	10.3462	ESO9	60	W	-0.0145	1.5002	Tethys
	10.3490	ESO10	60	W	-0.0144	1.5002	Tethys
	10.3504	ESO11	60	W	-0.0144	1.5002	Tethys
	10.3668	ESO12	60	W	-0.0139	1.4999	Tethys
	10.3696	ESO13	60	W	-0.0139	1.4999	Tethys
	10.3709	ESO14	60	W	-0.0138	1.4999	Tethys
	10.3940	ESO15	60	E	-0.0132	1.4995	Enceladus
	10.3948	ESO16	60	E	-0.0131	1.4995	Enceladus
	10.4180	ESO17	60	E	-0.0125	1.4992	Enceladus
	10.4217	ESO18	60	E	-0.0124	1.4991	Janus

Note. See Table I for the definitions of column headers.

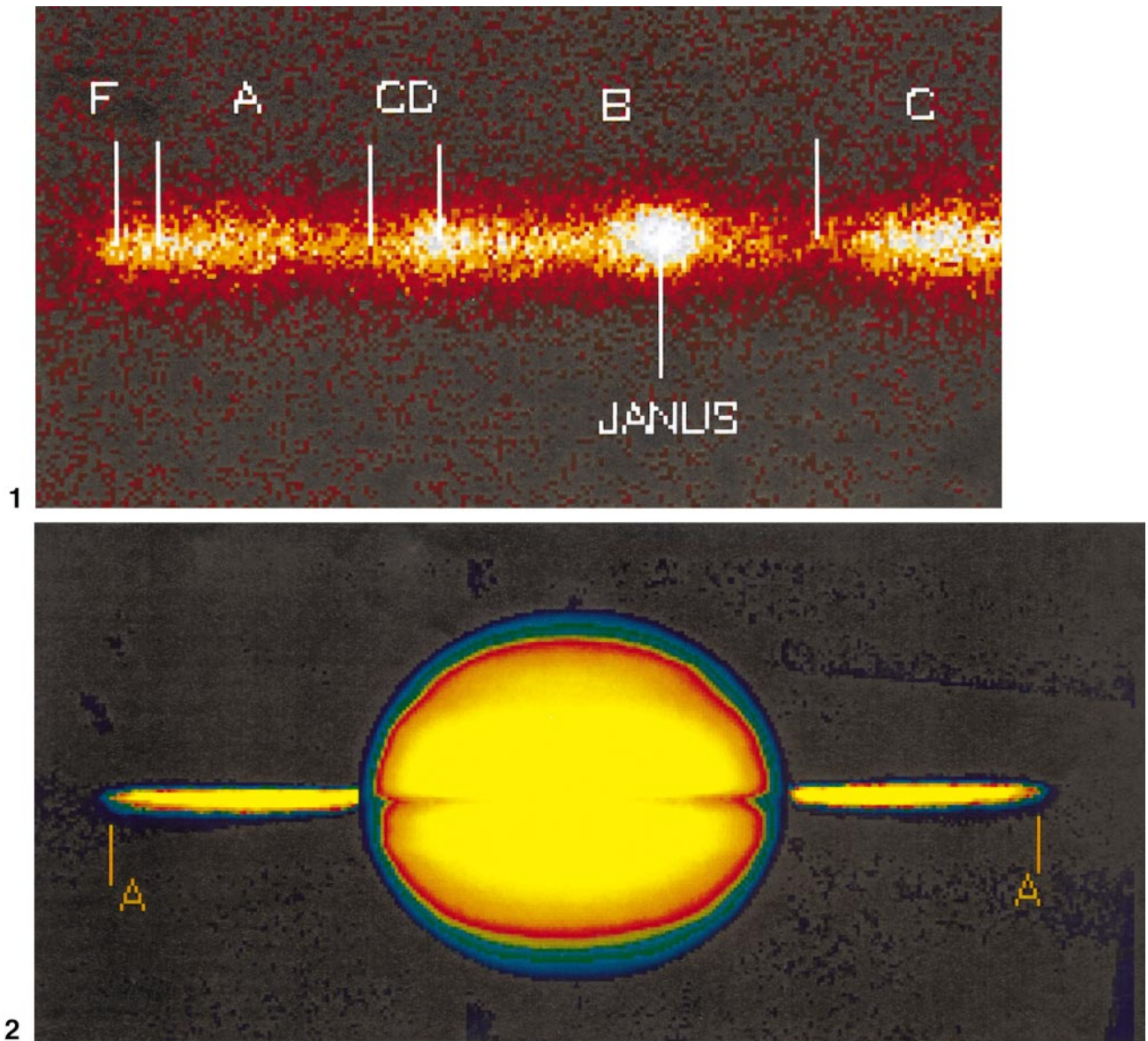


FIG. 1. An adaptive optics image taken in the K' band at the European Southern Observatory (ESO) showing the *dark* side of Saturn's rings on August 10, 1995, at 07:16:30 UT. The boundaries of the main rings are identified by vertical lines. Contrary to the HST images taken a few hours later, we still clearly detect the transmitted sunlight through the Cassini Division and the C ring. The image is 10.6×8.5 arcsec across, north is up, and east is left. The PSF is about 0.5 arcsec FWHM.

FIG. 2. A composite of images of the *lit* side of the rings taken on August 13, 1995 from Pic du Midi in the K band. The expected extremities of the A ring are shown by the two vertical lines. Contrary to Fig. 1, the brightness profile increases inward, from the A ring up to the C ring. No asymmetry of brightness between the two ansae is observed. The flux from the planet has been arbitrarily diminished to reduce the contrast with the rings. The image is 51.1×24.1 arcsec across, the seeing is 0.9 arcsec, north is up and east in left.

II.2. Data Reduction

II.2.1. Image Processing

Near infrared data. Although the flux detected from Saturn, its rings and, the satellites is dominated by the reflected sunlight in the near-infrared, there is a substantial terrestrial thermal background signal from the telescope and the sky. This background

signal was subtracted from single sky exposures taken immediately prior to or after the ring frames. The sky-subtracted frames were then corrected for pixel sensitivity variations using the flat-field exposures, from which dark-current frames were subtracted to remove electronic offsets. A specific periodic pattern was also removed by Fourier transforms from the Adonis images.

TABLE IIb
PIC Data (Lit Side)

Day	Exp	Profile	T	Ansa	B	B'	Calibration
August 12, 1995	12.0270	PIC1	4.61	W	0.0332	1.4754	SAO146846
	12.0580	PIC2	4.61	W	0.0332	1.4754	SAO146846
	12.0340	PIC3	4.61	E	0.0337	1.4753	SAO146846
August 13, 1995	13.0085	PIC4	4.61	W	0.0610	1.4609	SAO146846
	13.0089	PIC5	4.61	W	0.0610	1.4609	SAO146846
	13.0091	PIC6	4.61	W	0.0611	1.4609	SAO146846
	13.0158	PIC7	4.61	E	0.0612	1.4608	SAO146846
	13.0158	PIC8	4.61	W	0.0612	1.4608	SAO146846
	13.0161	PIC9	4.61	E	0.0612	1.4608	SAO146846
	13.0164	PIC10	4.61	E	0.0613	1.4608	SAO146846

Note. See Table I for the definitions of column headers.

The long exposures necessary for detecting the rings with a sufficient signal-to-noise ratio greatly increase the level of scattered light from the planet. Strong local gradients of brightness systematically bias the measurements on the rings. The background is determined from a robust, low-order, polynomial fit to each line parallel to the ring plane. Figure 3 shows two transverse scans (i.e., perpendicular to the line of the rings) from the ESO6 image before and after subtraction of the background.

The deconvolution technique using a PSF was not applied to the adaptive optics images. Direct deconvolution does not yield satisfactory results, so that an iterative procedure based upon the maximum likelihood algorithm was used, in particular to detect moving features in the rings (Poulet *et al.* 2000). However, this method is not suitable for photometry purposes since the flux is not conserved by this procedure.

HST data. The HST data used in this paper were calibrated data frames provided by the Space Telescope Science Institute. Conventional flatfielding and dark subtraction were performed during standard pipeline calibration (Biretta *et al.* 1996). The photometry was not corrected for small problems such as the charge transfer efficiency or the optical distortion over the field. The method of subtraction of the background is identical to that used for the near-infrared images.

II.2.2. Radial Profile Calibrations

For each ring scan, we perform astrometric and photometric calibrations. The edge-on profile defines the north-south location of Saturn's center. We calibrate radially the HST, Hawaii, and Pic profiles using Saturn's limb as the pointing reference.

TABLE IIc
HST Data (Dark and Lit Side)

Day	Exp	Profile	T	Ansa	B	B'
Dark side						
August 10, 1995	10.5747	HST1	260	E	-8.36×10^{-3}	1.4984
	10.5747	HST2	260	W	-8.36×10^{-3}	1.4984
	10.5797	HST3	260	E	-8.22×10^{-3}	1.4983
	10.5797	HST4	260	W	-8.22×10^{-3}	1.4983
	10.6380	HST5	260	E	-6.57×10^{-3}	1.4975
	10.7769	HST6	260	E	-2.65×10^{-3}	1.4954
	10.7804	HST7	300	E	-2.55×10^{-3}	1.4954
	10.7804	HST8	300	W	-2.55×10^{-3}	1.4954
	10.8387	HST9	300	E	-9.00×10^{-4}	1.4945
	10.8387	HST10	300	W	-9.00×10^{-4}	1.4945
	10.8443	HST11	300	E	-7.42×10^{-4}	1.4944
	10.8443	HST12	300	W	-7.42×10^{-4}	1.4944
Lit side						
August 10, 1995	10.9873	HST17	300	E	3.30×10^{-3}	1.4923
	10.9873	HST18	300	W	3.30×10^{-3}	1.4923
August 11, 1995	11.0478	HST19	300	E	5.01×10^{-3}	1.4914
	11.0478	HST20	300	W	5.01×10^{-3}	1.4914
	11.0517	HST21	14	E	5.12×10^{-3}	1.4914
	11.0517	HST22	14	W	5.12×10^{-3}	1.4914

Note. See Table I for the definitions of column headers.

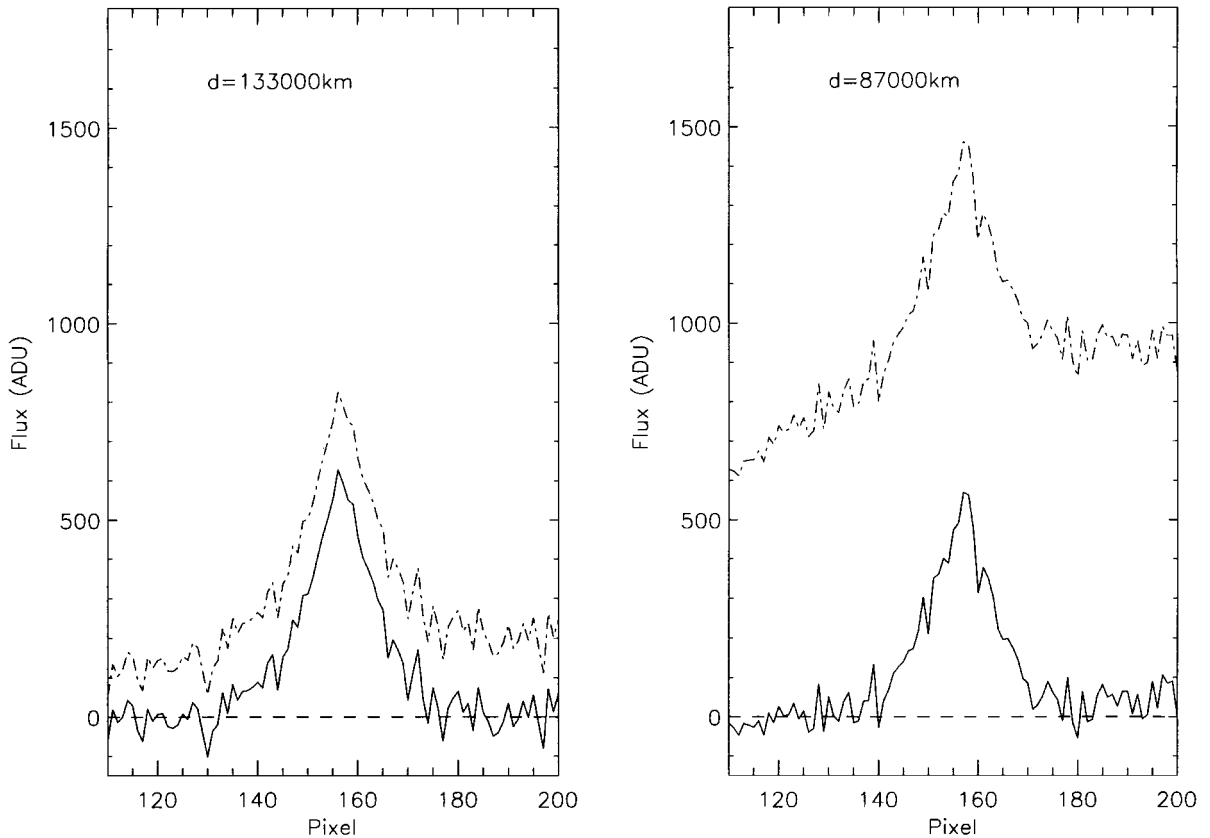


FIG. 3. Transverse scans in the A ring and in the C ring regions from an ESO image before (dotted-dashed line) and after (continuous line) the subtraction of the background. The latter has been determined from a robust low order polynomial fit. After calibration, the area under the curve is a measure of the edge-on brightness.

However, since the field of the adaptive optics camera is not wide enough to contain both ansae, the pixel coordinates of a reference satellite are then used for astrometric calibration. The pixels of each scan are then binned according to the radius.

The photometric calibration of groundbased data was achieved by using the satellites available on the image. The magnitude of the satellites were calibrated against the UKIRT faint standard stars FS26, FS29, FS30 (Casali and Hawarden 1992), and SAO146846. The calibration was made at an airmass similar to that of the satellite images. We ignored color corrections between the K and K' magnitudes. The resulting mean magnitudes and associated uncertainties are listed in Table III. They are scaled to the mean Saturn opposition distance, but remain uncorrected for unknown phase effects. Magnitudes derived for Enceladus, Hyperion, and Janus agree with previous values (Cruikshank 1980, Bauer *et al.* 1997). Tethys

and Dione are redder than the values reported by Cruikshank (1980).

Figure 3 shows that the background, once subtracted, does not represent the largest source of uncertainty of the ring brightness. The largest uncertainty actually comes from the satellite photometry in the case of groundbased data. Moreover, no systematic study on the stability and photometric calibration has been done for adaptive optics data. Lai (1996) indicates that it is preferable to make relative photometry. However, since our goal is to produce an estimate of the ring thickness, we are more interested in absolute photometry. In particular, we reduce the uncertainties due to the variations of seeing by using a photometric reference in the field.

The absolute photometric calibration for the HST data are discussed in Nicholson *et al.* (1996). We use their conversion factors to calibrate the data.

TABLE III
Satellite Photometry in K Filter (at Mean Opposition)

Satellite	Tethys	Dione	Enceladus	Hyperion	Janus
Magnitude	9.50 ± 0.06	9.42 ± 0.08	11.08 ± 0.10	12.90 ± 0.15	13.67 ± 0.20

Once this was done, we used the following procedure to process the data. First, each ring image is sliced into narrow transverse scans, perpendicular to the ring plane. The value of the raw analogic data units (ADU) along the scan is then, after calibration, a measure of the integrated edge-on brightness I/F of the rings, averaged over each pixel. Here is I the intensity received from the rings and πF is the incident solar flux received at Saturn. Each transverse scan is then fitted by a gaussian curve, with two adjustable parameters: the area under the curve and the FWHM. The area yields the “equivalent photometric thickness” Z at the location of the scan,

$$Z(d, \lambda) = \int \frac{I}{F} dH \quad \text{km}, \quad (1)$$

where H is the height above the ring plane in km. Hence, Z would be the physical thickness of the ring if the edge of the latter were a perfectly reflecting Lambert surface illuminated from normal incidence (i.e., an edge with a geometric albedo equal to unity). Note that in principle Z does not depend upon the point spread function of the instrument, from conservation of energy. In practice, however, the signal-to-noise ratio deteriorates as the signal from the rings is diluted into many pixels, due to the presence of the background, photon noise, etc. Note also that Z does depend on the wavelength of observation, λ , through the dependence of the photometric properties of the particles upon λ .

By repeating the scans, we eventually obtain the equivalent thickness Z of the rings as a function of the projected distance d to Saturn's center. Practically and for all data sets, the uncertainties due to the background contributions are smaller than the uncertainties associated with the satellite photometry for distances d larger than 80,000 km.

III. PHOTOMETRIC MODEL

III.1. Ring Models

We now relate the reflectance I/F of the rings to the particle photometric properties and to the ring optical depth, τ . In fact, the value of I/F is a sum of contributions from various rings j observed at the same projected distance d . So

$$Z(d) = \sum_j Z_j(d), \quad (2)$$

each ringlet being defined by its geometrical shape and its optical depth.

We assume that the A and B rings have constant optical depths of 0.6 and 1.5, respectively, independent of the wavelength and of the distance to Saturn's center (Esposito *et al.* 1984). Since the elevation of Earth on the ring plane was very low during the observations, these parameters have actually a small influence, and these approximations result in a substantial saving of computation time. The C ring and the Cassini Division have a mean optical depth $\tau \sim 0.1$ (Esposito *et al.* 1984). However, the presence of diffuse sheets of material with optical depth $\tau \sim \mu$

in these two regions could add substantial contributions to the transmitted light. To allow for this possibility, and to explore the sensitivity of the results to the presence of such material, we also solve for the optical depth in these regions.

The profiles of the dark side of the rings indicate that the contribution of the F ring to Z is important (Nicholson *et al.* 1996 and Bosh *et al.* 1997). Furthermore, we shall see (Section IV.2.2) that the flux from the F ring as observed on the lit side or the dark side are similar. Except for the possibility of a fortuitous value of the F ring's optical depth, this means that the residual flux is probably due to a thick ribbon, rather than to a narrow flat ring.

The optical depth profiles of the F ring derived from the Voyager photopolarimeter and radio occultation experiments show considerable variations with radial distance and with wavelength (Showalter *et al.* 1992). The azimuthal profiles show likewise very large variations (Kolvoord *et al.* 1990, Nicholson *et al.* 1996). To simplify the scattering calculations as much as possible, we idealize the F ring as a ribbon of physical height H and width $W = R_{\text{ext}} - R_{\text{int}}$ as illustrated in Fig. 4.

Olkin and Bosh (1996) detected a small inclination of $0.0063 \pm 0.0016^\circ$ for the F ring. This inclination is likely to complicate the interpretation of the residual flux. In particular, it is not yet clear whether the discrepancy observed between the two ansae is due to the F ring, and/or to a global warp of the ring plane. Taking into consideration these two phenomena requires the knowledge of some physical quantities of the F ring (radial optical depth, physical height) and some geometric characteristics of the warp. Some of these parameters will be derived from our modeling. In addition, we expect that the F ring inclination and the eventual warp of the main rings affect more the lit side profiles than the dark side profiles, which will allow us to derive the ring thickness. In fact, we will see that these approximations shall not change our conclusions. Consequently, we did not model them.

III.2. Scattering by the Main Rings

III.2.1. Radiative transfer model. We describe the rings as a plane-parallel, homogeneous, scattering layer. Since no detectable discontinuity in the ring brightness is seen during the Earth RPX either at the radius corresponding to the outer edge of the A ring or at the radius of the Mimas 5:3 bending wave (Nicholson *et al.* 1996), we neglect the flux from the outer “vertical” edge of the main rings. Then, there are three different sources of light which contribute to the brightness:

- The sunlight directly reflected by the ring plane. This contribution is dominant when we observe the lit side.
- The sunlight transmitted through the ring plane. This contribution may be dominant in certain tenuous regions of the dark side with $\tau \sim \mu$.
- The light scattered by the disk of Saturn, then reflected and transmitted off the rings (Saturn shine). This contribution is relevant only on the dark side.

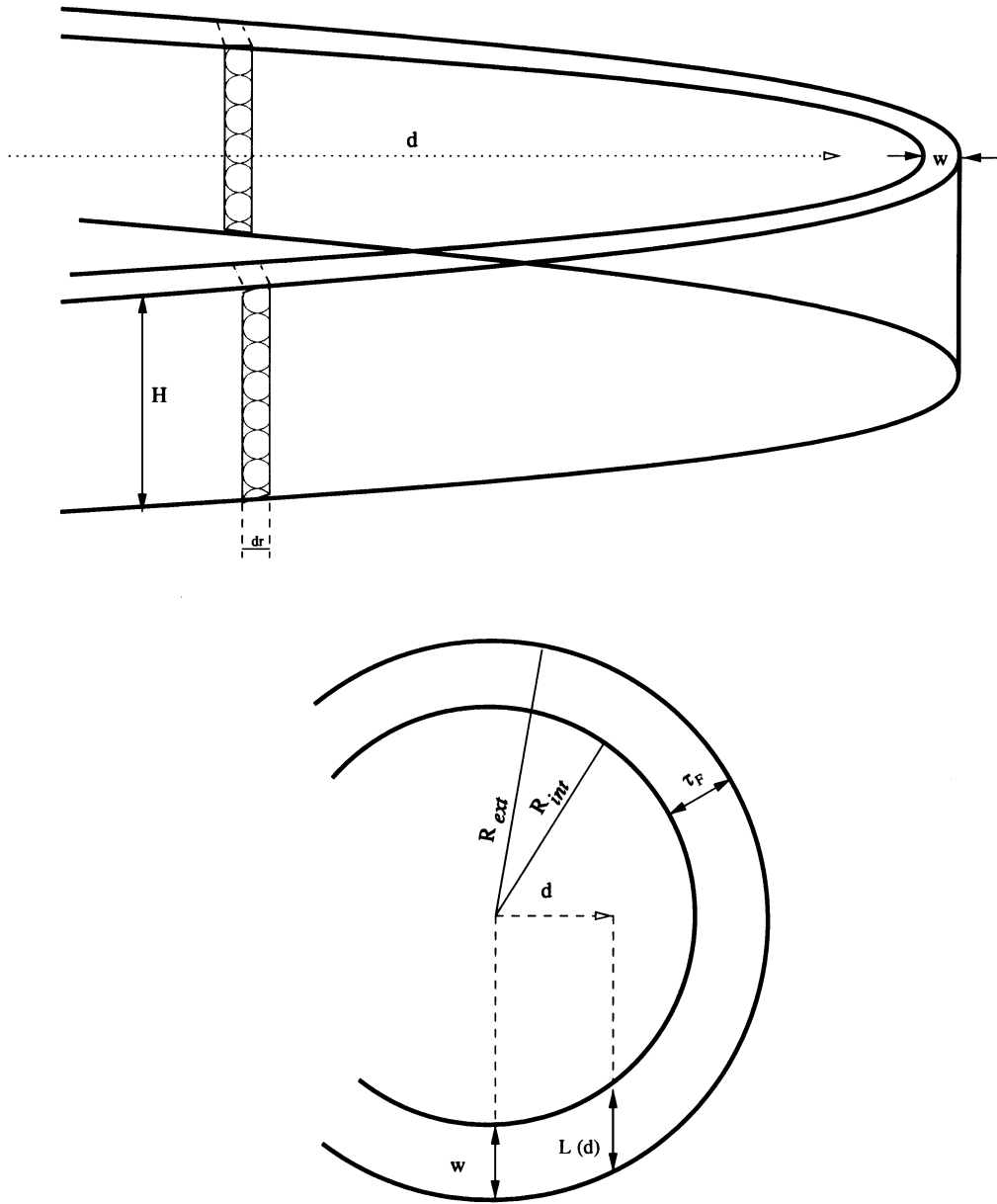


FIG. 4. The ribbon model of the F ring with physical height H , radial width W , inner radius R_{int} , and outer radius R_{ext} . (Top) The thickness has been magnified compared to the radial dimension. (Bottom) A pole-on view of the model.

We can use the equations of radiative transfer for a plane-parallel medium with normal optical depth τ to derive the singly scattered reflected light (Chandrasekhar 1960),

$$\frac{I}{F} = \frac{1}{4} \frac{\mu'}{\mu + \mu'} P(\alpha) \left\{ 1 - \exp \left[-\tau \left(\frac{1}{\mu'} + \frac{1}{\mu} \right) \right] \right\}, \quad (3)$$

and the singly scattered transmitted light,

$$\frac{I}{F} = \frac{1}{4} \frac{\mu'}{\mu - \mu'} P(\alpha) \left\{ \exp \left(-\frac{\tau}{\mu} \right) - \exp \left(-\frac{\tau}{\mu'} \right) \right\}, \quad (4)$$

where $P(\alpha) = \omega_0 \times g(\alpha)$ is the scattering function for particles of Bond albedo ω_0 and phase function $g(\alpha)$.

Figure 5 displays the intensity of singly scattered transmitted sunlight by isotropic particles of albedo unity, in the geometry of the Earth RPXs. The elevation of the Sun being constant, the singly transmitted sunshine depends on τ and B only. This diagram shows that regions with optical depths comprised between $\mu \equiv \sin B$ and $\mu' \equiv \sin B'$ are mostly responsible for the singly transmitted sunlight at small tilt angles. We could then expect a possible contribution of transmitted light from the zone between the A and the F rings in HST images, because μ can be smaller than the optical depth of this zone $\tau \sim 10^{-4}$ (Showalter

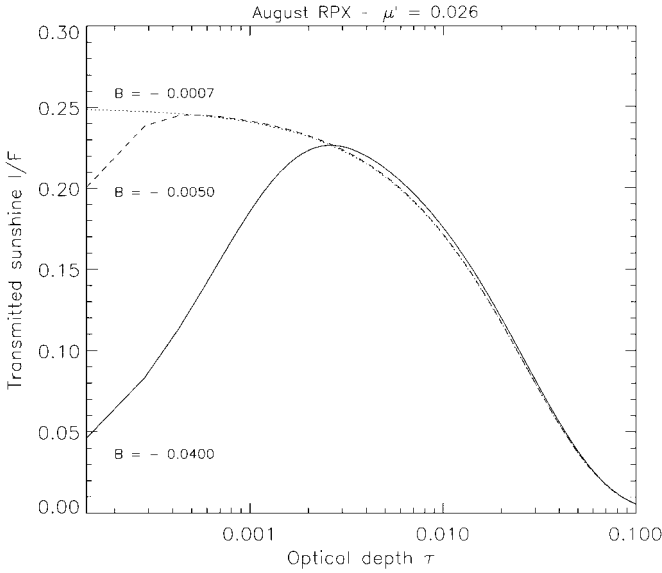


FIG. 5. Singly transmitted sunshine vs the normal optical depth τ for three sub-Earth latitudes B ($\mu \equiv \sin B$) on the ring plane, computed for the August RPX geometry.

et al. 1998). If this transmitted light was a significant part of the signal, its contribution would vary with ring location and with time due to dependence of projected area on distance from Saturn. Such clear trends were not detected. Therefore, we can assume that the residual flux was not due to transmitted light from this zone, at least very near the RPX exact time. For the Cassini Division, we assumed a constant optical depth. In practice, we solve for the optical depth of this region when fitting the observed profiles.

Multiply scattered light can be estimated by assuming isotropy, using Chandrasekhar's functions X and Y , which are found by iterations applied to the integral equations (Chandrasekhar 1960). We solve for the isotropic multiple reflection and transmission, respectively, in the limit of $\mu \rightarrow 0$:

$$\frac{I}{F} \sim \frac{1}{4} \omega_0 [X(\mu') - 1] \quad (5)$$

$$\frac{I}{F} \sim \frac{1}{4} \omega_0 \left[Y(\mu') - \exp\left(-\frac{\tau}{\mu'}\right) \right]. \quad (6)$$

Note that assuming isotropy for the backscattering Saturn's rings causes a modest overestimate of multiple scattering.

Light scattered off the planet can yield a significant contribution to the ring brightness. We use an approximation method by assuming that Saturn's clouds scattering function obeys a Minnaert law. The Minnaert law does not represent any physical model based on radiative transfer theory, but it provides an acceptable fit to the data (Karkoschka and Tomasko 1992, Westphal *et al.* 1992, Ortiz *et al.* 1995). The intensity emitted at the center of a surface element dA follows the law (Dones *et al.*

1993)

$$\frac{I}{F}(dA) = R_0 \cos^k(i) \cos^{k-1}(\epsilon), \quad (7)$$

where i is the angle of incidence and ϵ the angle of reflection on the element of surface dA , k is the limb-darkening coefficient, and R_0 is the reflectance associated with $\cos i = \cos \epsilon = 1$. By applying this formula, we obtain the normalized flux $F(dA)/F$ reflected by dA and received by a ring particle located at the projected distance d . The various solutions for the reflected light by the rings [Eqs. (3) and (5)] and for the transmitted light through the rings [Eqs. (4) and (6)] can be used, with μ' depending on the element of surface dA and on the distance d . To estimate the brightness resulting from the Saturn shine $(I/F)_S$, we finally calculate the integral,

$$\left(\frac{I}{F}\right)_S = \int_A \left[\frac{I}{F(dA)}\right] \left[\frac{F(dA)}{F}\right] dA, \quad (8)$$

requiring that the surface element dA of Saturn is both illuminated by the Sun and is visible from the ring particle. The limb-darkening of the northern hemisphere of Saturn at $0.89 \mu\text{m}$ exhibits temporal changes, implying considerable variations in the physical parameters of the tropospheric clouds (Ortiz *et al.* 1995). Moreover, no studies in the near infrared have been done so far. For all data, we take a value k averaged over the latitudes, namely $k = 1$ (Ortiz *et al.* 1995), which corresponds to Lambert's law. For the HST narrowband methane filter centered at a wavelength of $0.89 \mu\text{m}$, the geometric albedo of the planet is equal to $p \sim 0.1$ (Karkoschka 1998); this gives $R_0 = p(k + \frac{1}{2}) \sim 0.15$. For the K and K' bands, we use the albedo ($p \sim 0.05$) given by Clark and McCord (1979).

III.2.2. Phase function and single scattering albedo. Part of the photometric data were modeled using the two parameters ω_0 and $g(\alpha)$, which are known within reasonable bounds. Extensive works have been done by Dones *et al.* (1993) and Doyle *et al.* (1989) to model the visible ($0.50 \mu\text{m}$) photometric properties of the A and B rings, respectively. These studies show that rough-surface, macroscopic particles (1 cm–10 m) are responsible for the bulk of the ring reflectivity. As the A and B rings seem to contain very little free micrometric dust, the same property is probably true for the Cassini division and the C ring (Cooke 1991).

In practice, the photometric properties of the main rings are modeled by the *product* of the single scattering albedo ω_0 by the phase function $g(\alpha)$ from the lit side profiles. For macroscopic particles, ω_0 is the spherical albedo of the particle taken as a whole, ignoring diffraction. Since these large particles are probably covered by a layer of smaller particles, the large particle albedo actually is related to the spherical albedo of the particles composing the regolith. For instance, Van de Hulst (1974) derived ω_0 as a function of the properties of the grains covering the macroscopic particle, using a semi-infinite atmosphere model.

Original ring radial profiles (from 0.3 to 0.9 μm) have been obtained from HST images (Poulet *et al.* 1999). They show that the rings are quite red, implying a strongly wavelength-dependent albedo ω_0 . We find averaged geometric albedos of 0.44 ± 0.06 for the A ring, 0.64 ± 0.08 for the B ring, 0.12 ± 0.06 for the C ring, and 0.22 ± 0.05 for the Cassini Division, i.e., about 20% larger than the geometric albedos at 0.5 μm . These albedos correspond to a surface made of contaminated water ice. The geometric albedo at 0.89 μm of the B ring corresponds to a single scattering albedo of ~ 0.55 by assuming the phase function independent of wavelength (see below a discussion about this hypothesis).

Since the single scattering albedo at 0.89 μm is relatively well constrained, this facilitates the determination of $g(\alpha)$. Unfortunately, there are more uncertainties for the 2.2- μm data. We use then the spectrum $\omega_0(\lambda)$ of Saturn's main rings from Clark *et al.* (1986) normalized to the B ring albedo at the V band.

The scattering behavior of the main rings determined at visual wavelength from Voyager images is similar to that of most atmosphereless satellites, e.g., the moon of the galilean satellites (Dones *et al.* 1993). However, as the albedo, the particle phase function $g(\alpha)$ may also vary with wavelength. This issue is discussed by Cuzzi and Estrada (1998). There is no evidence of wavelength-dependence for ring particle phase function, at least over the visual spectral region. On the other hand, recent and preliminary analysis of HST images of Saturn's rings and Voyager images shows that the main rings are more strongly backscattering at shorter wavelengths (UV and blue) than at longer wavelengths (red and near-IR) (referee's communication). In our case, the range of phase angle (3.55° and 5.55°) is too small to derive precisely the phase function. However, we are able to measure the product $\omega_0 \times g(\alpha)$. Thus, fixing the more accurate parameter (here, ω_0), we adjust the value of the phase function to match the observed reflectivities of the lit side profiles. This method gives a first approximation of the phase function that is unknown at the studied wavelengths. Moreover, this allows us to incorporate the derived values of $\omega_0 \times g(\alpha)$ in our modeling of the dark side, which diminishes the number of parameters in this stage. To compare our results with previous works, a power-law phase function is used (Ockert *et al.* 1987),

$$g(\alpha) = c_n(\pi - \alpha)^n, \quad (9)$$

where n is a positive constant and c_n is a constant which normalizes the integral of the phase function over 4π steradians. Large values of n correspond to steeper backscattering phase functions.

III.3. Scattering by the F Ring

III.3.1. Radiative transfer model. As discussed earlier, the observed profiles require a proper modeling of the F ring scattering properties. We recall that the F ring is modeled as a physically thick ribbon of height H and radial width W (Fig. 4). We neglect multiple scattering and assume that the F ring is viewed edge-

on. Adopting the same notation as in Section III.2 and in Fig. 4, we obtain the intensity reflected by the F ring at the projected distance d from Saturn's center,

$$\frac{I}{F} = \frac{P(\alpha)}{8} \{1 - \exp[-2\tau_t(d, W)]\}, \quad (10)$$

where $\tau_t(d, W)$ is the transverse (integrated along the line of sight) optical depth associated with the integrated physical width $L(d)$ of the ring. The quantity $\tau_t(d, W)$ can be expressed as a function of the radial optical depth τ_F (along W) of the F ring as

$$\tau_t(d, W) = \rho \tau_F \frac{L(d)}{W}. \quad (11)$$

The factor ρ depends on whether the far arm of the F ring is fully obscured ($\rho = 1$) or fully visible behind the closest F ring's arm and the main rings ($\rho = 2$). This ring model tends to become optically opaque near the extremities because of the effect of mutual shade between the particles. The intensity approaches its maximum for $d = R_{\text{int}}$, where $\tau_t = \rho \tau_F [1 + (2R_{\text{int}}/W)]^{1/2}$. Since $R_{\text{int}} \gg W$, the line-of-sight optical depth $\tau_t \gg 1$, and so the sensitivity of I/F to W is very small. From now, we take $W = 50 \pm 5$ km, which defines the width of the strand $F\gamma$, the brightest component of the F ring (Murray *et al.* 1997).

III.3.2. Phase function and albedo. We divide the F ring particles into two populations: small particles with sizes comparable to the wavelength, and macroscopic particles of much larger sizes. The large particles can dominate the intensity at low phase angles, while providing a negligible contribution at high phase. We model the phase function g_{large} with the same empirical function as defined for the main rings (Eq. (9)). The fractional contribution f of the dust to the F ring optical depth in the Voyager images is larger than about 90% (Showalter *et al.* 1992).

Although its phase function shows a strong forward-scattering property, the dust can also contribute to the backscattered light. For small spherical particles of given size and refractive index, we can derive the phase function g_{dust} and albedo ω_{dust} from Mie theory. We assume that the size distribution of this population obeys a power-law variation with an index $q = -4$, close to the value derived by Showalter *et al.* (1992). During the RPX events, the intensity scattered in Mie scattering reaches a maximum for the size parameter $x = 2\pi r/\lambda$ comprised between 10 and 50 (Throop and Esposito 1998). This range corresponds to particles radius $3 \lesssim r \lesssim 20$ μm (resp. $1 \lesssim r \lesssim 7$ μm) at $\lambda = 2.2$ μm (resp. $\lambda = 0.89$ μm). To take into account the effects of particles with small radius r , we have considered a population with lower and upper cutoffs in size of 0.1 and 20 μm (corresponding to $0.3 \lesssim x \lesssim 60$ at $\lambda = 2.2$ μm).

The composition of the F ring particles is presently unknown, and we assume here a water ice composition. To allow for the presence of contaminants, we also introduce an imaginary component of the index, equal to $10^{-3}\sqrt{-1}$ (Throop and Esposito 1998). While the phase functions of pure water ice and of slightly

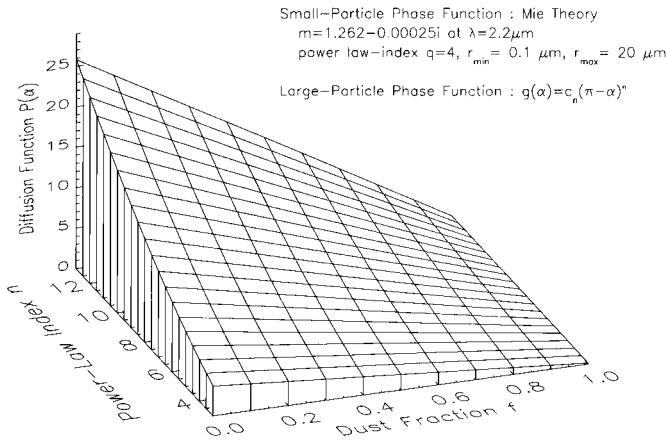


FIG. 6. The scattering function $P(\alpha)$ (Eq. (12)) of the F ring vs two parameters of our F ring model: the dust fraction f and the exponent n describing the large particle phase function (Eq. (9)). Here, we take $\alpha = 0^\circ$. The Mie theory provides the single albedo ω_{dust} and the phase function g_{dust} for spherical particles with the refractive index of pure water ice at $2.2 \mu\text{m}$, and we use Van de Hulst's theory to derive the Bond albedo ω_{large} .

contaminated water ice are almost similar, any contaminant influences the average albedo. The choice of the albedo for the large particles, ω_{large} , is also critical because it governs the fraction of large particle in the F ring. Assuming that large particles are covered by dust, the single scattering albedo of large particles is derived from Van de Hulst's theory. Finally, the scattering function $P(\alpha)$ of a mixture of dust and large particles is given by

$$P(\alpha) = f\omega_{\text{dust}}g_{\text{dust}}(\alpha) + (1-f)\omega_{\text{large}}g_{\text{large}}(\alpha). \quad (12)$$

Figure 6 displays the dependence of $P(\alpha)$ on f and n , from which it follows that the contribution of the F ring is highly sensitive to the dust fraction f via $P(\alpha)$.

Combining (1), (9), (10), (11), and (12), we deduce the F ring photometric thickness:

$$Z(d) = [f\omega_{\text{dust}}g_{\text{dust}}(\alpha) + (1-f)\omega_{\text{large}}c_n(\pi - \alpha)^n] \times \frac{H}{8} \left\{ 1 - \exp\left[-2\frac{\rho\tau_{\text{F}}L(d)}{W}\right] \right\}. \quad (13)$$

The observations provide $Z(d)$, and the model of the F ring is described in the right-hand side of the equation above. The model has four free parameters: the radial optical depth, τ_{F} , the fraction of dust, f , the power-law index of the large particle phase function, n , and the physical height of the F ring, H . As stated above, the contribution of the F ring is highly sensitive to the dust fraction f .

IV. ANALYSIS

The geometry of each image (emission angle, incidence angle and distance from Saturn's center) and convolution by the seeing

are taken into account in each model, so that the thickness Z values may be directly compared with the observations.

IV.1. Expected Contributions to the Ring Thickness

To give some preliminary indications of the expected brightness of the rings in different geometries, we have performed light scattering calculations for the geometries of images HST7 (Table IIc) and ESO1 (Table IIa). The photometric thickness was computed at $d = 100,000 \text{ km}$ for various value of τ . Otherwise, we assume a phase function with $n = 1.8$ and an albedo $\omega_0 = 0.55$ for the B ring particles and $n = 3$ for the F ring particles, with a dust fraction $f = 0.80$ and a physical thickness $H = 20 \text{ km}$. Only one ansa is taken into account ($\rho = 1$). The values used here come from the fits of the observed profiles (see the next sections). The results are shown in Fig. 7.

Very close to the RPX (geometry of HST7 image), the reflected light from the F ring overwhelms all other contributions for radial optical depths $\tau_{\text{F}} > 0.05$. For optical depths lower than 0.05, the observed brightness is dominated by the singly transmitted sunlight, but only for locally thin parts of the main rings. For $\tau > 0.16$, the Saturn shine dominates all contributions, except that of the F ring. Figure 7 also shows that the contribution of the F ring approaches a constant value for radial optical depths τ_{F} larger than a few tenths.

For a larger value of $|B|$ (bottom panel, geometry of ESO1 image), the Saturn shine and transmitted sunlight increase relative to the F ring component which stays constant. However, it appears that the F ring and transmitted sunlight through the Cassini Division and C ring are still important and that all other terms can be yet neglected. The Saturn shine and transmitted light increasing with $|B|$, we expect these components to dominate the ring's brightness for larger values of $|B|$. We do not have available data more a few days away from the RPX. A set of HST images resulting from an observing program by M. Tomasko and E. Karkoschka (Program ID 6030) and taken on August 6, 1995, shows that the brightening due to the sunlight transmitted through the translucent C ring and Cassini Division dominates clearly the inner sections of profiles. However, our calculations show that the Saturn shine always remains lower than the F ring brightness during the period of the dark side between May and August RPXs, so that the F ring should still dominate in the outer sections for all the values of B ($0^\circ < B < 0.6^\circ$). This is quite plausible because the August 6 flux outside the Cassini Division remains very low.

It remains to be seen whether the F ring may be opaque enough to dominate the edge-on ring brightness. Figure 8 shows the F ring contribution to Z vs d , for various radial optical depths τ_{F} and for $\rho = 2$, using the model described by Eq. (13). The inner sections of the profiles are more sensitive to the radial optical depth than the outer ones. We see that the profiles tend to become flatter for increasing radial optical depths. In practice, we solve for τ_{F} for each observed profile.

It is well known that the F ring is not azimuthally symmetric: its brightness can vary by a factor 2 or more. For instance, several

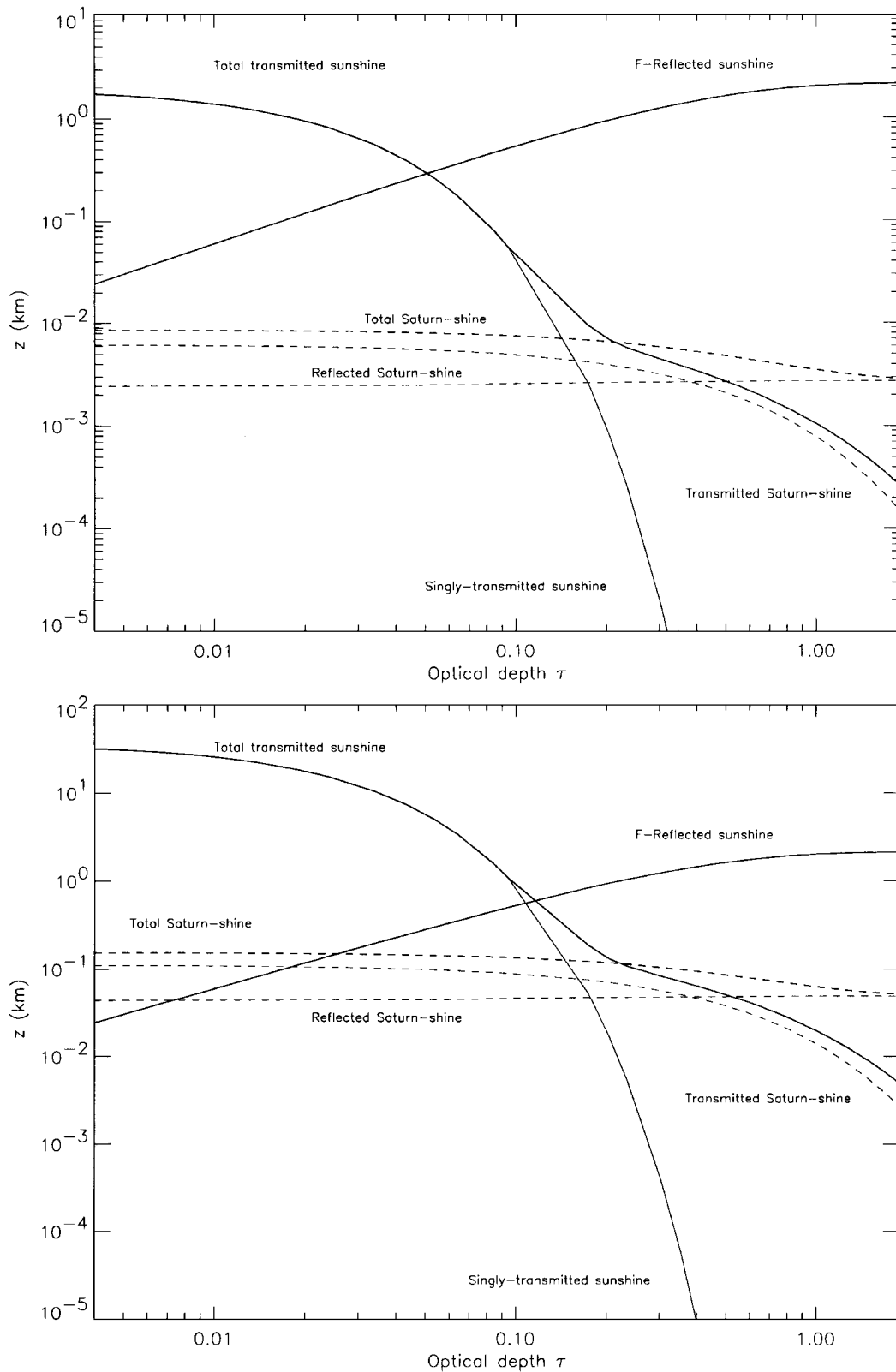


FIG. 7. (Top) Contributions of the sunlight, the Saturn shine, and the F ring to the photometric thickness Z as a function of optical depth τ in the viewing geometry of image HST7 (Table IIc). Here, the optical depth of the F ring is the *radial* optical depth τ_F (integrated along the radial width W , see Fig. 4). The contributions of the sunlight and the Saturn shine are calculated by taking into account the projected surface of the B ring at $d = 100,000$ km. (Bottom) The same as above, but in the viewing geometry of image ESO1. Apart from the F ring contribution which stays constant, all the other contributions increase.

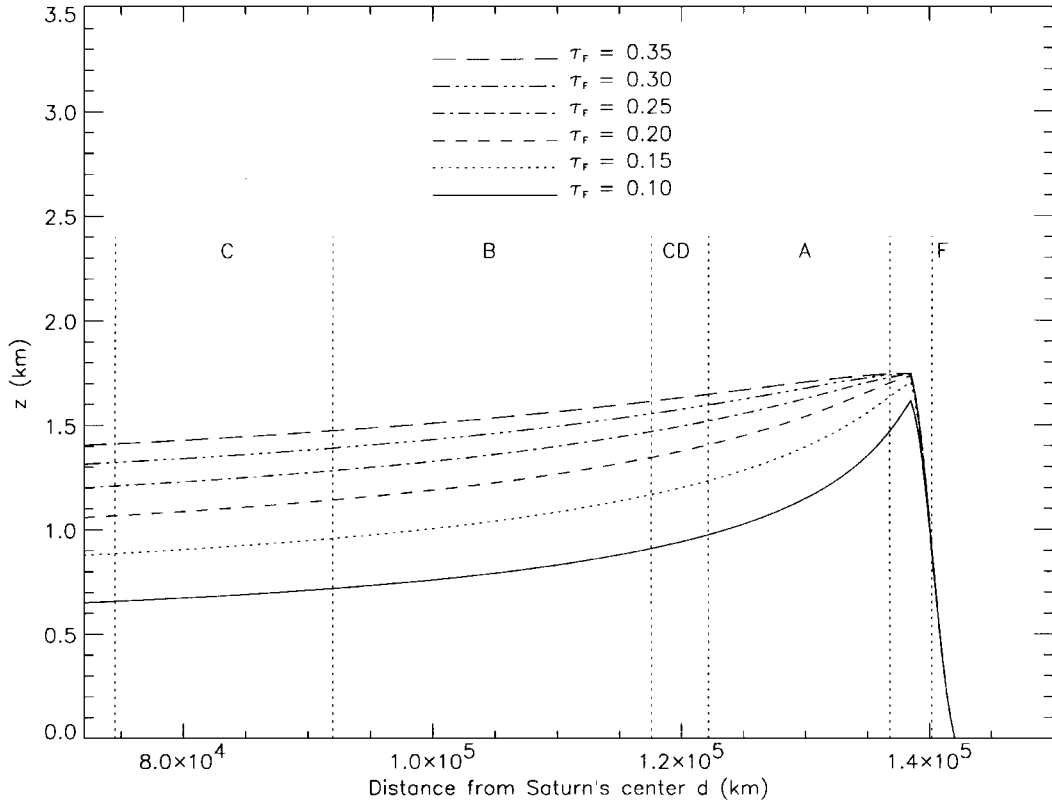


FIG. 8. Contributions of the F ring to Z as a function of the distance d , for various radial optical depths. Both contributions of the near and far ansae are taken into account here (which corresponds to taking $\rho = 2$ in Eq. (11)). The value of τ_F has to be multiplied by 2 if only one ansa is detected, in order to have the same plots.

condensations of matter orbiting close to the F ring have been detected in the images. They could be explained by a concentration of matter which corresponds to a local increase of the radial optical depth τ_F . So, it would be perhaps preferable to make τ_F azimuth dependent. This work was done in Poulet *et al.* (2000). Here, we prefer to keep τ_F azimuth independent, without considering in the fits the parts which show local bumps (clumps of matter) or local dips (gaps of matter). Consequently, the derived value τ_F must be considered as a mean value, not affected by local longitudinal variations. The large longitudinal variations (a few tens of degrees in length) influence our modeling, and they are part of the errors on τ_F .

On the lit face, the singly scattered sunlight totally dominates the intensity reflected by the rings, so that the reflectivity is approximately equal the product of particle albedo and phase function. Indeed, the intensity of the reflected sunlight by single diffusion does not depend on the optical depth because τ/μ is large (Eq. (3)). In this case, we use the data to determine the photometric properties of the main rings.

IV.2. Modeling of the Lit Side

IV.2.1. IR data. The observations of the lit side (Table IIb) are sensitive only to the main rings, so that we use them to con-

strain the phase function of the large particles, with the values of albedos derived in Section III.2.2. By fitting theoretical profiles to the observations, we determine the exponent n of the phase function of large particles for given fixed albedos of each ring.

There are no significant variations of brightness between the rings. For a single-scattering albedo of 0.50, the best fit is obtained for $n = 1.65^{+0.20}_{-0.10}$. Conversely, assuming $n = 3$, ω_0 must be equal to 0.28 ± 0.03 , a value consistent with the Bond albedo determined by the normalized spectrum of Saturn's main rings (see Section III.2.2.). This latter combination of parameters will be our preferred one.

IV.2.2. HST data. We now apply the same procedure as before with a better knowledge of the single scattering albedo of the main rings. The higher spatial resolution of HST images allows us to separate more easily the contribution of the different rings. The signal does not drop at the outer edge of the A ring, but continues up to the radius of the F ring. The fits to the profiles showing the lit side (profiles HST17 to HST22; see Table IIc) give the relation between the albedo and the large particle phase function as shown in Table IV. All the single scattering albedos used here are taken from Nicholson and Dones (1991). These values are for $\lambda = 0.5 \mu\text{m}$, but considering that the geometric

TABLE IV
Possible Ranges of n and ω_0 for the Main Ring Particles^a

Location	ω_0	n
Ring A	0.4–0.6	2.8–1.8
Ring B	0.4–0.6	2.45–1.5
Ring C	0.12–0.3	2.3–0.5
Cassini division	0.2–0.4	2.8–1.25

^a From the fits of HST profiles of the lit side at $\lambda = 0.89 \mu\text{m}$, see text.

albedos at $0.89 \mu\text{m}$ are only 20% larger than those at $0.5 \mu\text{m}$, we think that the large range of values tabulated by Nicholson and Dones (1991) are appropriated for our study.

The derived values of n are not consistent with the value $n \sim 3$ derived from Voyager images (Doyle *et al.* 1989, Dones *et al.* 1993). This suggests that the main rings are less strongly backscattering at longer wavelengths (near-IR) than at shorter wavelengths. This result could be due to the particular geometry of observations with very grazing light. However, as mentioned in Section III.2.2, similar property has been detected in usual conditions (open rings). Further observations would be needed to confirm this phenomenon, for which we do not have an explanation at the moment.

Note finally that the geometric albedo is surprisingly low: $p \sim 0.4$ from $\omega_0 \sim 0.55$ and $n \sim 1.8$. The ring albedo varies by 30% within phase angles of $0\text{--}6^\circ$ and with ring tilt (Franklin and Cook 1965, Lumme and Irvine 1976). Published ring spectrum by Karkoschka (1994) at 2.7° phase angle, i.e., with phase angle similar to that of our observations, gives a full-disk albedo equal to 0.45. This value is close to our measurements.

IV.3. Modeling of the Dark Side in May and August

In later calculations, the photometric properties (ω_0 and n) of the main rings particles have been fixed at constant values, as determined above. We fit 10 Hawaii profiles (Table I), 18 ESO profiles (Table IIa), and 12 HST profiles (Table IIc), all showing the dark side. Remember that the F ring contribution depends on four variables: (1) the fraction of dust f , (2) the exponent n defining the large particle phase function, (3) the physical height H of the F ring, and (4) the radial optical depth τ_F .

IV.3.1. Contribution of the Cassini Division. The contribution of this gap can be more important (Figs. 1 and 7) than the F ring contribution, but it is spatially confined near $d \sim 120,000$ km. We match the bumps of the profiles at this location by fitting the optical depth of the Cassini Division. Each observed bump represents an average over the light transmitted by the different parts of Cassini Division. The May data can detect regions with a normal optical depth of 0.09 ± 0.01 , while the August images reveal material with an optical depth of 0.050 ± 0.006 . Note that only B' varies between the two observations (Tables I and IIa). The lower value obtained in August

stems from the fact that a smaller of μ' allows one to detect a smaller τ .

As one gets closer to the RPX time, the profiles become essentially featureless with respect to d . Only the first HST images in our set (~ 7 h before the crossing) show an increase of flux at the location of the Cassini Division, and also at the inner part of the C ring. The profiles at these locations are not regular and smooth, contrary to what is observed at Hawaii and ESO. For the latter images, B is larger and the resolution worse than for the HST images. This implies that only a small part of these regions must scatter the solar light. We derive an optical depth of 0.014 ± 0.01 for the inner C ring, consistent with the optical depth of certain zones near and inward of the Maxwell and Colombo gaps (Esposito *et al.* 1983b). However, the strong fluctuations of the profiles (due to clumps, subtraction of the background, cosmic rays) result in large relative uncertainties.

Some zones in the Cassini Division, with a mean optical depth of 0.037 ± 0.01 , also scatter light. These values confirm that there are some regions in the Cassini Division and in the C ring with optical depth lower than 0.10.

IV.3.2. Radial optical depth τ_F . Using the HST data alone, the best fits to the profiles give a radial optical depth of $\tau_F = 0.16 \pm 0.05$ for the F ring, assuming $\rho = 2$ (or 0.32 ± 0.1 assuming $\rho = 1$, see Eq. (11)). The new objects detected in the HST profiles (Nicholson *et al.* 1996), orbiting near or in the F ring, are visible even if they orbit on the far arm of the F ring. This suggests that the two arms contribute to the photometric thickness. We find higher but consistent values using the Hawaii data ($\tau_F = 0.19 \pm 0.05$, $\rho = 2$) and the ESO data ($\tau_F = 0.27 \pm 0.10$, $\rho = 2$).

The derivation of τ_F combined with the physical width $W = 50 \pm 5$ km (Murray *et al.* 1997) allow us to compute the equivalent depth $D = \int \tau(a) da = 8 \pm 3$ km at $0.89 \mu\text{m}$. Our result differs from the value $D = 4.33 \pm 0.13$ km at $0.264 \mu\text{m}$ inferred by Showalter *et al.* (1992) from Voyager data. This could indicate a red color for the F ring, but Poulet *et al.* (1999) measured a blue-neutral color between 0.3 and $0.7 \mu\text{m}$. However, we think that the HST value is consistent with the Voyager value. First, the values are almost consistent within the errors bars.¹ In addition, the radial profile of the optical opacity at $0.264 \mu\text{m}$ corresponds to a scan in a particular region of the F ring. Then, we expect the opacity to vary with longitude, which could explain the difference between the two estimations of D .

We have explored the contribution of the tenuous sheet of material between the F ring and the outer edge of the A ring. Nicholson *et al.* (1996) have already claimed that such material cannot be the major source of the residual flux. Our modeling confirms also this fact. Indeed, since the parameter W modifies

¹ D at $0.89 \mu\text{m}$ becomes more consistent with the value $D = 5.0 \pm 0.3$ km at $0.5 \mu\text{m}$ (Showalter *et al.* 1992).

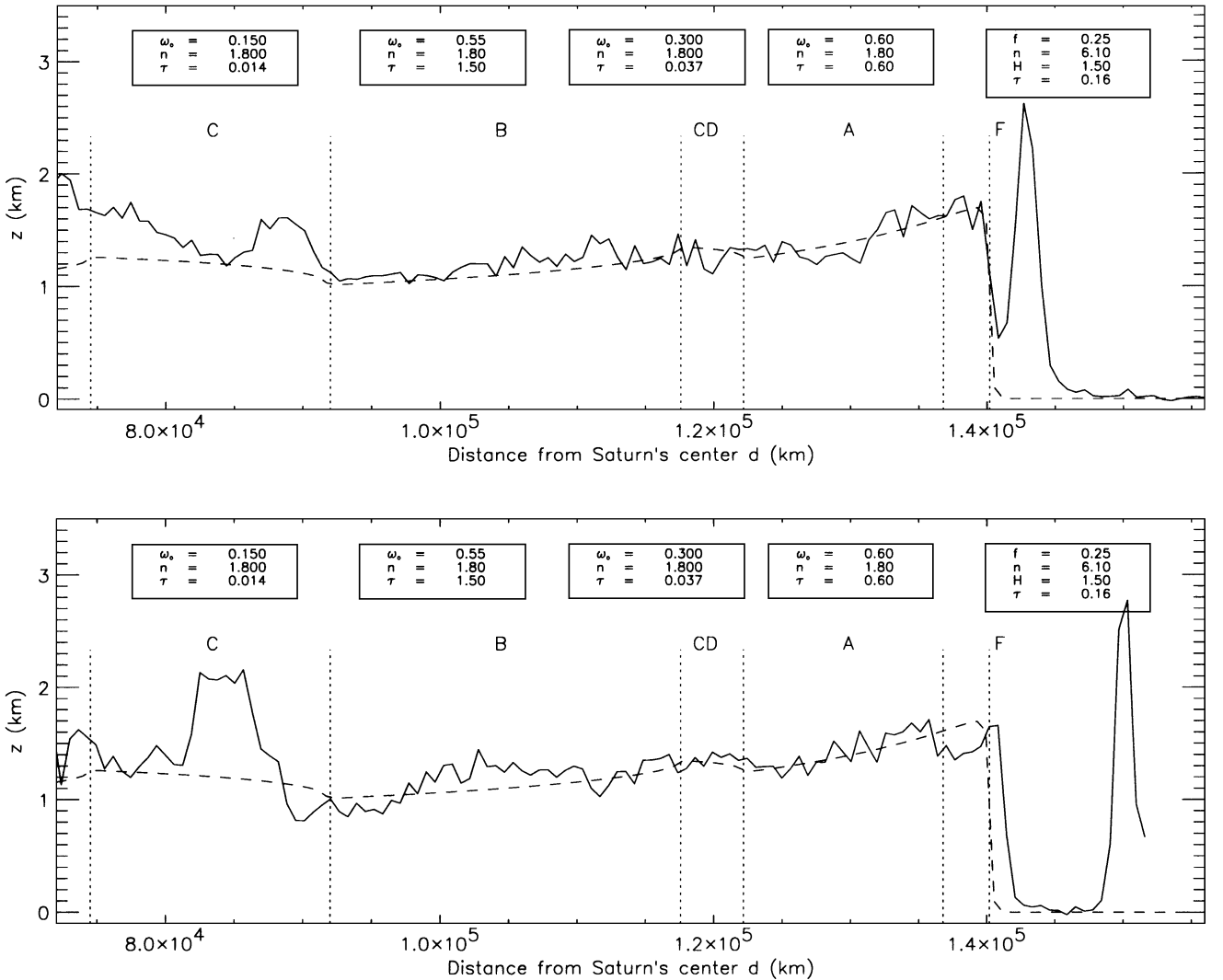


FIG. 9. The photometric thickness Z as a function of distance d , for two images taken by HST (see Table IIc) showing the dark side of the rings. (Top) Profile derived from HST7 image; (bottom) profile derived from HST9 image. The top (respectively bottom) profile is modified by the object 1995/S 5 (respectively Pandora) at about 88,000 km (respectively 84,000 km). The dashed curves represent the best-fit model obtained for all the HST profiles. The sets of parameters used for each ring are indicated in the boxes. For the F ring, τ_F denotes the *radial* optical depth (here the two ansae are taken into account), while for the main rings, it corresponds to the *normal* optical depth. The choice of parameters for the F ring corresponds to a potential solution in the space of parameters (H, f, n) . Supplementary constraints on these parameters are introduced in Section IV.3.4.

very little the retrieved profiles (Section III.3.1), we can estimate the normal optical depth of the sheet $\tau_{\text{sheet}} = \tau_F H / W$ in order to match the photometric profiles. Taking $W_{\text{sheet}} = 3400$ km (the distance between the A and the F rings defining the Pioneer gap), $\tau_F = 0.2$, and $H = 20$ km (derived below), we get $\tau_{\text{sheet}} \gtrsim 10^{-3}$. This value is incompatible with the upper limit of 10^{-4} quoted by Showalter *et al.* (1998).

IV.3.3. Preliminary solutions for H, n, f . Figure 9 shows an example of fits to some HST profiles, assuming that the F ring particles are made of slightly contaminated water ice. We indicate the parameters (ω_0, n, τ) used for the main ring components and the combination of parameters (f, n, H) used for

the F ring. For any composition approaching pure water ice, the value of n decreases.

The various fits yield the possible values of n as a function of the physical height H for different fractions of dust f (Fig. 10). We have tested dust fractions f between 0 and 98%,² and physical heights H between 1.0 and 40.0 km. If the large particles have surface properties similar to that of the main ring particles (i.e., $n < 4$), this implies that H is larger than 2.0 km. One can see that whatever the wavelength of observation and the

² The case $f \sim 100\%$, which is straightforward because independent of n , implies unrealistic values of H between 50 and 100 km.

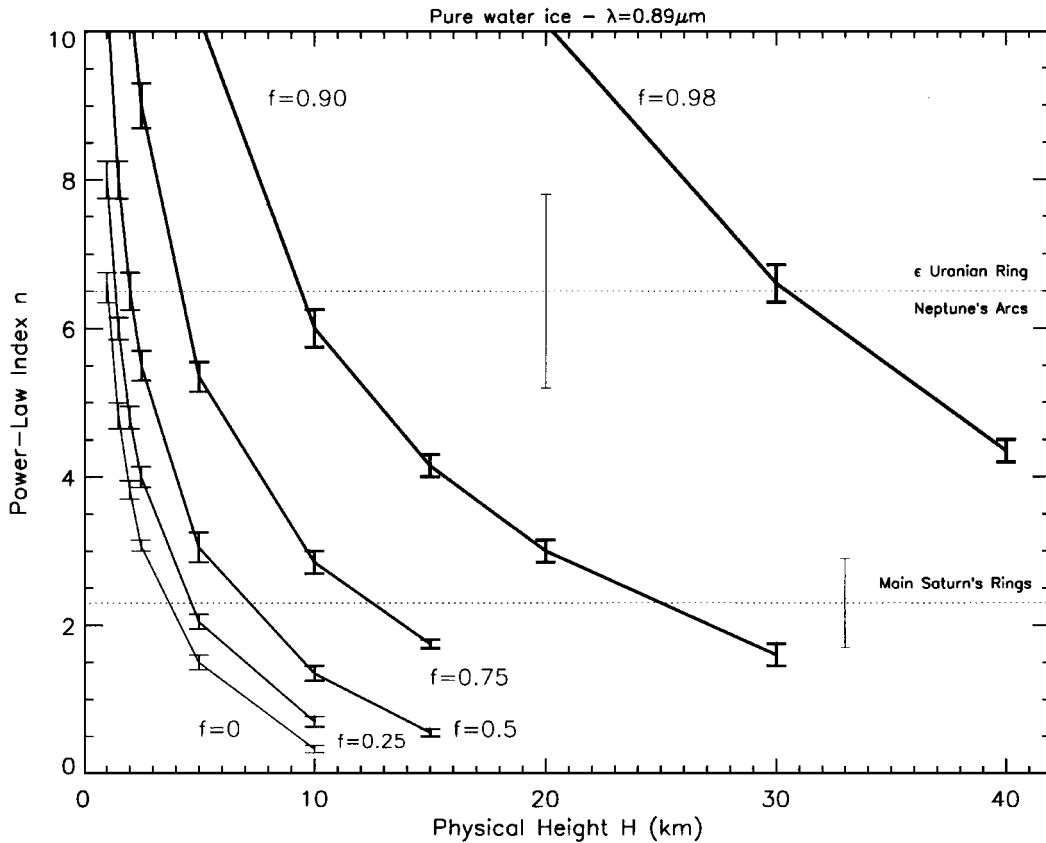


FIG. 10. Relation between the power-law index n of the phase function of the large particles in the F ring vs the physical height H of the F ring, and for various dust fractions f . Each curve fits the photometric profiles Z observed at $\lambda = 0.89 \mu\text{m}$. The composition of particles are assumed to be pure water ice. We plot also the values of n for the particles of the ϵ uranian ring (Karkoschka 1997), Neptune's arcs (Ferrari and Brahic 1994), and the main rings (this study).

composition of the particles are, the values of n remain unrealistically large ($n > 4$) for dust fraction larger than 50% and physical height smaller than 2–3 km.

Two extreme scenarios can explain the edge-on brightness of the F ring, and so the edge-on residual flux of the whole system. First, if we suppose that large bodies dominate the scattering properties of the F ring, then these bodies have to be distributed vertically over more than 2 km. The Voyager radio occultation experiments provide direct evidence that some large bodies must be present in a F ring core (Showalter *et al.* 1992). However, this core is very narrow (width < 1 km), so it is difficult to understand how it may have such a large vertical distribution.

By contrast, an envelope of micrometer-sized particles can dominate the F ring brightness ($f > 0.5$), and so explain the edge-on residual flux of Saturn's rings. In this case, this envelope (assumed to be ~ 50 km wide) must have a vertical scale larger than 5 km. In this case, we agree with the conclusion of Showalter *et al.* (1992), who claim that small particles dominate the ring's scattering behavior even in backscattering light.

Finally, we note that the taking into consideration the inclination of the F ring will not change our conclusions, because the main ring contributions are almost insignificant. By contrast, a warp of the main rings could diminish the F ring contribution

by obscuring parts of the far arm of the F ring. The main ring should be then visible in these sections. Except for the possibility of fortuitous values of comparable brightness, we would expect the profiles to vary with distances; but this is not the case.

IV.3.4. Further modeling of the F ring thickness. In the previous section, we have examined various solutions for the parameters describing the F ring particles: the dust fraction f , the power-law index n of the macroscopic particle phase function, and the physical height H . All these parameters influence the photometric thickness, and the effect of one of them can be compensated by the others.

We now derive H . We reduce the number of free parameters by fixing the value of n . The phase function of large particles is based on the behavior of icy satellites and of the main ring particles. Hence, by taking $n = 3 \pm 1$, we deduce from Fig. 10 the relation $H(f)$, which is plotted in Fig. 11. The knowledge of the F ring normal optical depth ($\tau_N = 0.074$ derived from Model 1 of Showalter *et al.* 1992), combined to our determination of the radial optical depth, τ_F , yields H , through $H = W(\tau_N/\tau_F)$. This expression can be rephrased in term of equivalent depth D as $H = D/\tau_F$. We indicate in Fig. 11 the regions corresponding to different range of widths W .

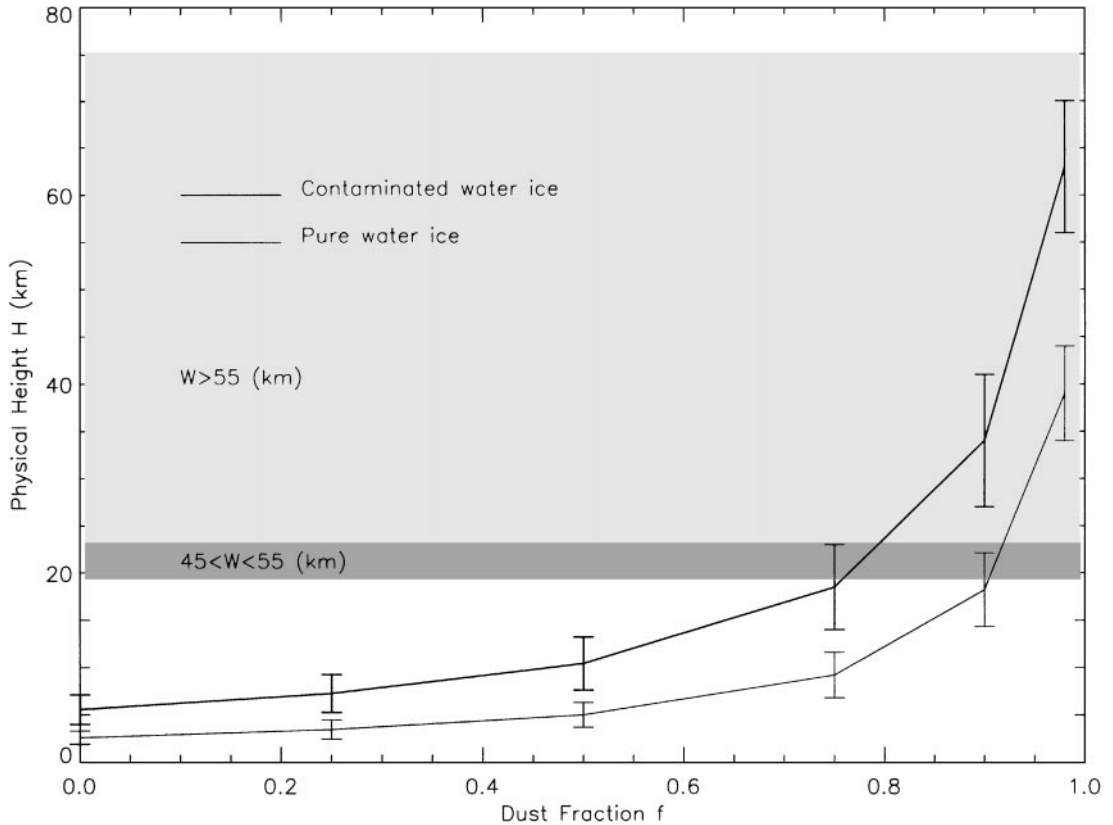


FIG. 11. The relation $H(f)$ obtained from Fig. 10, by fixing the value $n = 3 \pm 1$. We also plot the curve corresponding to the case of contaminated water ice (thick line). Thus, fixing the width W , we can read the respective heights H which verify the relation $H = W\tau_N/\tau_F$, where τ_N is the normal optical depth of the F ring. Considering a F ring envelope of width $W = 45\text{--}55$ km, our model indicates a vertical thickness of about 20–22 km, composed by at least 80% of dust particles.

It appears that the value $W = 50 \pm 5$ km is obtained for a physical height $H = 21 \pm 4$ km. Note that the corresponding values of dust fraction is then $f = 0.80 \pm 0.03$ (respectively $f = 0.90 \pm 0.02$) for contaminated water ice (respectively pure water ice). They are similar to the values obtained by Showalter *et al.* (1992).

Use of the normal optical depth $\tau_N = 0.074$ measured from the photopolarimeter (PPS) experiment for our purpose could have important limitations, because we cannot be sure that the longitude of the PPS is typical of the ring as a whole. So we consider two other models of profiles (Model 2 and 4 of Showalter *et al.* 1992) which fit the Voyager data almost as well as the Model 1 measured from the PPS profile. The relation $H = D/\tau_F$ implies $H = 25 \pm 5$ km for Model 2 and $H = 28 \pm 6$ km for Model 4. Hence, $H = 21 \pm 4$ km may be a lower limit, although it remains our preferred value, because Model 1 represents the best fit to the Voyager data (Showalter *et al.* 1992).

IV.4. Evolution of the Ring Brightness

The profiles from ESO and PIC images allow us to follow the evolution of the ring brightness with time over 4 days spanning the exact time of the August RPX (Fig. 12). We perform a linear

least squares fit of the data from the before and after the crossing. As expected, the precrossing slope is slightly negative because the brightness is decreasing slowly as all the components except for that of the F ring become less visible. We extrapolate the fit at the exact time of Earth's transit to find that the minimum signal is not zero. We recall that this thickness does not represent the actual physical thickness of the rings, but that it is caused by the F ring. The postcrossing slope is positive and much larger than the precrossing slope since the lit side of Saturn's rings becomes more and more visible. Our data are not accurate and numerous enough to detect a difference of brightness between east and west ansa. However, we obtain a good representation of the evolution of Z at $d = 100,000$ km before and after Earth's transit. The values that we use for the parameters discussed above are $n = 3$, $\omega_0 = 0.28$ for the main rings, $\tau_F = 0.27$, $H = 20$ km, $f = 0.9$, and $n = 3$ for the F ring. We can note, on the other hand, that the intersections of the linear fits from before and after the crossing with the exact time of RPX do not give the same brightness. This discrepancy may be due to the fact that the homogenous plane parallel scattering layers assuming for the main rings are not a satisfactory model at very low tilt angles. This could thus explain why the geometric albedos derived from HST images of the lit side are so low (see Section IV.2.2.).

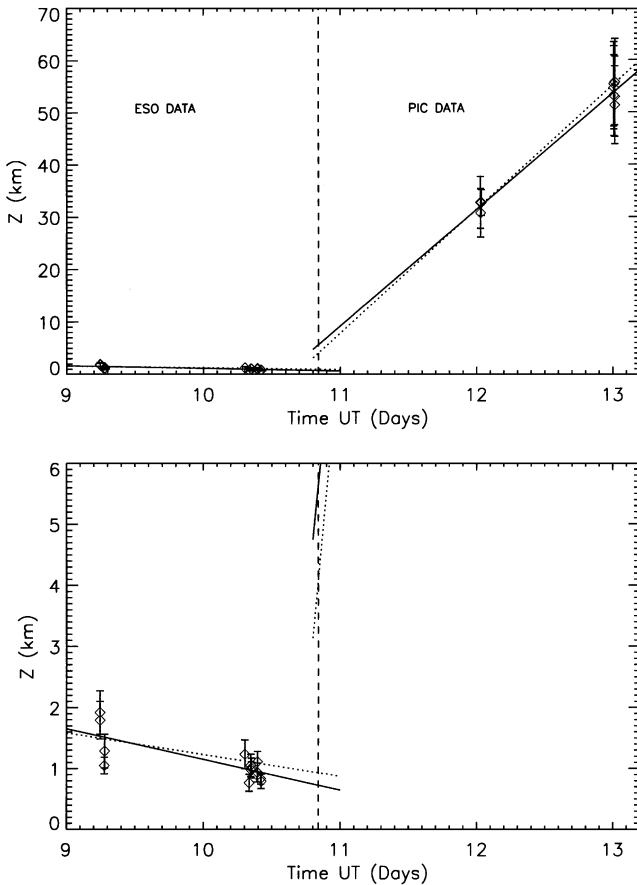


FIG. 12. (Top) The equivalent photometric thickness Z of the main rings vs time during the 10 August 1995 RPX in the near-IR. Z was scanned at $d = 100,000$ km, but averaged over 96,000 to 104,000 km to improve the signal-to-noise ratio. The results are derived from ESO (before RPX) and PIC (after RPX) observations. Linear least-squares fits to the data from before and after the transit are shown as solid line. By fixing the photometric properties of the rings (see text), we model the evolution of Z , which is shown as the dotted lines. The vertical dashed line indicates the crossing mean time (Nicholson *et al.* 1996). (Bottom) The same as above, but with a modified vertical scale to show the photometric evolution of the unlit profiles.

V. CONCLUSION AND FUTURE WORKS

The edge-on brightness of Saturn's rings is due to different components, but the observed profiles and their basic evolution with time can be explained by a physically thick F ring with a ribbon structure (Fig. 4).

This ribbon is characterized by its physical height, H , dust fraction, f , phase function of large particles via the exponent, n (Eq. (9)), and radial optical depth, τ_F (Eq. (11)). The Earth RPX alone provides τ_F (Section III.3.2) and a lower limit for H (Section III.3.3). Taking into account the normal optical depth and the width of the main strand of the F ring, as derived from the Voyager data (Showalter *et al.* 1992, Murray *et al.* 1997), we can constrain more stringently the vertical structure of the F ring. We then infer a physical thickness of $H = 21 \pm 4$ km.

Kolvoord and Burns (1992) have demonstrated that a slightly inclined satellite can excite the F ring's particles in an observable fashion. The maximum Δi (kick in inclination) from a ring particle-satellite encounter can reach 5×10^{-3} degrees, yielding an out-of-plane displacement of more than 10 km. Olkin and Bosh (1996) detected an inclination of the F ring equivalent to a displacement of 15 ± 4 km, which is close to our derivation. It remains to be seen at that point how these displacements can explain an effective thickness of the same order, in particular against the damping effect of frequent collisions.

Our best fits indicate that the dust dominates the scattering properties of the F ring, even at small phase angles. However, these observations also provide evidence that a fraction of about 10–20% of larger bodies must be present in the region of the F ring. As stressed by Showalter *et al.* (1992), these bodies are present at least in the narrow core of the F ring. Poulet *et al.* (2000), on the other hand, propose a dynamical model for the origin of the F ring clumps. In this model, parent bodies (hundred meters to kilometer in size) collide, ejecting regolith, which are later swept up by other parent bodies. These ejecta clouds can also have typical heights of 20 km or so.

Finally, Salo (1987) estimates that gravitational encounters can maintain an equilibrium thickness for the F ring of the order of several times the radii of the largest particles. A rough estimation of the radii R of the largest bodies located at radial distance a is given by

$$R \sim \frac{H}{5} \left(\frac{a_R}{a} \right)^{3/2}, \quad (14)$$

where a_R is the Roche radius. For the F ring ($H \sim 20$ km), R could reach a few kilometers, a value consistent with the largest values derived by Poulet *et al.* (2000).

Our light-scattering model does not go beyond the classical assumptions, which treat the main rings as a homogeneous and plane parallel slab, many particle thick, essentially vanishing behind a ribbon-like F ring near the RPX. This model explains reasonably well the profiles observed very close to the RPX, but a more complete modeling of the F ring can be envisaged by adding different effects such as the inclination, the shadow effect from the main rings, or the presence of several 3-D braids. Also, further theoretical studies are needed to address the presence of large bodies and transient clumps in the F ring. The high resolution and temporal coverage of the Cassini orbiter could greatly help resolving some of these issues.

ACKNOWLEDGMENTS

It is a pleasure to acknowledge useful discussions with P. D. Nicholson, C. Pantin, and F. Colas. This work was supported by the French Programme National de Planétologie and by the Université Paris VI. Helpful comments were obtained from the referees L. Dones and L. W. Esposito.

REFERENCES

- Bauer, J., J. J. Lissauer, and M. Simon 1997. Edge-on observations of Saturn's E and G rings in the near-IR. *Icarus* **125**, 440–445.
- Biretta, J. A., C. Burrows, J. Holtzman, I. Heyer, M. Stevens, S. Baggett, S. Casertano, M. Clampin, A. Fruchter, H. Ferguson, R. Gilliland, R. Griffiths, J. Krist, K. Noll, C. O'Dea, M. Stiavelli, A. Suchkov, J. Surdej, and B. Withmore 1996. *WFPC2 Instrument Handbook*, Version 4.0. Space Telescope Science Inst., Baltimore, MD.
- Bosh, A. S., A. S. Rivkin, J. W. Percival, M. Taylor, and G. W. Van Citters 1997. Saturn ring-plane crossing, May 1995: Pole precession and ring thickness. *Icarus* **129**, 555–561.
- Burns, J. A., P. Hamill, J. N. Cuzzi, and R. H. Durisen 1979. On the “thickness” of Saturn's rings caused by satellite and solar perturbations and by planetary precession. *Astron. J.* **84**, 1783–1801.
- Casali, M. M., and T. G. Hawarden 1992. A set of faint JHK standards for UKIRT. *JCMT-UKIRT Newsl.* **4**, 33.
- Chandrasekhar, S. 1960. *Radiative Transfer*. Oxford Univ. Press, Oxford.
- Clark, R. N., and T. B. McCord 1979. Jupiter and Saturn: Near-infrared spectral albedos. *Icarus* **40**, 180–188.
- Clark, R. N., F. P. Fanale, and M. J. Gaffey 1986. Surface composition of natural satellites. In *Satellites* (J. A. Burns and M. S. Matthews, Eds.), pp. 437–491. Univ. of Arizona Press, Tucson.
- Cooke, M. L. 1991. *Saturn's Rings: Radial Variation in the Keeler Gap and C Ring Photometry*, Ph.D. dissertation. Cornell University, Ithaca, NY.
- Cruikshank, D. P. 1980. Near-infrared studies of the satellites of Saturn and Uranus. *Icarus* **41**, 240–245.
- Cuzzi, J. N., and P. R. Estrada 1998. Compositional evolution of Saturn's rings due to meteoroid bombardment. *Icarus* **132**, 1–35.
- Dollfus, A. 1979. Photometric determination of the Saturn rings' thickness. *Astron. Astrophys.* **75**, 204–206.
- Dones, L., J. N. Cuzzi, and M. R. Showalter 1993. Voyager photometry of Saturn's A ring. *Icarus* **105**, 184–215.
- Doyle, L. R., L. Dones, and J. N. Cuzzi 1989. Radiative transfer modeling of Saturn's outer B ring. *Icarus* **80**, 104–135.
- Esposito, L. W., N. Borderies, P. Goldreich, J. N. Cuzzi, J. B. Holberg, A. L. Lane, R. B. Pomphrey, R. J. Terrile, J. J. Lissauer, E. A. Marouf, and G. L. Tyler 1983. Eccentric ringlet in the Maxwell gap at 1.45 Saturn radii multi-instrument Voyager observations. *Science* **222**, 57–60.
- Esposito, L. W., J. N. Cuzzi, J. B. Holberg, E. A. Marouf, G. L. Tyler, and C. C. Porco 1984. Saturn's rings: Structure, dynamics, and particle properties. In *Saturn* (T. Gehrels and M. S. Matthews, Eds.), pp. 463–545. Univ. of Arizona Press, Tucson.
- Esposito, L. W., M. O'Callaghan, and R. A. West 1983. The structure of Saturn's rings—Implications from the Voyager stellar occultation. *Icarus* **56**, 439–452.
- Ferrari, C., and A. Brahic 1994. Azimuthal brightness asymmetries in planetary rings. I. Neptune's arcs and narrow rings. *Icarus* **111**, 193–210.
- Franklin, F. A., and A. F. Cook 1965. Optical properties of Saturn's rings. II. Two-color phase curves of the 2 bright rings. *Astron. J.* **70**, 704–720.
- Hénon, M. 1982. A simple model of Saturn's rings. Revisited. In *Anneaux des planètes* (A. Brahic, Ed.), 363–384. Centre National d'études Spatiales, Toulouse.
- Ip, W.-H. 1995. Implications of meteoroid-ring interactions for observations of the 1995 Saturn RPX. *Icarus* **117**, 212–215.
- Karkoschka, E. 1994. Spectrophotometry of the jovian planets and Titan at 300- to 1000-nm wavelength: The methane spectrum. *Icarus* **111**, 174–192.
- Karkoschka, E. 1997. Rings and satellites of Uranus: Colorful and not so dark. *Icarus* **125**, 348–363.
- Karkoschka, E. 1998. Methane, ammonia, and temperature measurements of the jovian planets and Titan from CCD-spectrophotometry. *Icarus* **133**, 134–146.
- Karkoschka, E., and M. G. Tomasko 1992. Saturn's upper troposphere 1986–1989. *Icarus* **97**, 161–181.
- Kolvoord, R. A., and J. A. Burns 1992. Three-dimensional perturbations of particles in a narrow planetary ring. *Icarus* **95**, 253–264.
- Kolvoord, R. A., and J. A. Burns, and M. R. Showalter 1990. Periodic features in Saturn's F ring: Evidence for nearby moonlets. *Nature* **345**, 695–697.
- Lai, O. 1996. *L'optique adaptative du télescope CFH et son utilisation pour l'étude des coeurs de galaxies à flambée d'étoiles*. Thèse de doctorat de l'Université de Paris VII.
- Lissauer, J. J. 1985. Bending waves and the structure of Saturn's rings. *Icarus* **62**, 433–447.
- Lumme, K., and W. M. Irvine 1976. Photometry of Saturn's rings. *Astron. J.* **81**, 865–893.
- Murray, C. D., M. K. Gordon, and S. M. G. Winter 1997. Unraveling the strands of Saturn's F ring. *Icarus* **129**, 304–316.
- Nicholson, P. D., and L. Dones 1991. *Rev. Geophys. Supplement*, pp. 313–327. U.S. National Report to International Union of Geodesy and Geophysics 1987–1980.
- Nicholson, P. D., M. R. Showalter, L. Dones, R. G. French, S. M. Larson, J. J. Lissauer, C. A. McGhee, P. Seitzer, B. Sicardy, and G. E. Danielson 1996. Observations of Saturn's ring-plane crossings in August and November 1995. *Science* **272**, 509–515.
- Ockert, M. E., J. N. Cuzzi, C. C. Porco, and T. V. Johnson 1987. Uranian ring photometry: Results from Voyager 2. *J. Geophys. Res.* **92**, 14969–14978.
- Olkin, C. B., and A. S. Bosh 1996. The inclination of Saturn's F ring. *Bull. Am. Astron. Soc.* **28**, 1125.
- Ortiz, J. L., F. Moreno, and A. Molina 1995. Saturn 1991–1993: Clouds and hazes. *Icarus* **117**, 328–344.
- Poulet, F., E. Karkoschka, and B. Sicardy 1999. Spectrophotometry of Saturn's small satellites and rings from HST images. *J. Geophys. Res.* **104**, 24,095–24,110.
- Poulet, F., B. Sicardy, P. D. Nicholson, E. Karkoschka, and J. Caldwell 2000. Saturn's ring-plane crossings of August and November 1995: A model for the new F-ring objects. *Icarus* **144**, 135–148.
- Salo, H. 1987. Numerical simulations of collision between rotating particles. *Icarus* **70**, 37–51.
- Showalter, M. R., J. A. Burns, and D. P. Hamilton 1998. Saturn's “Gossamer” ring: The F ring's inner sheet. *Bull. Am. Astron. Soc.* **30**, 1044.
- Showalter, M. R., J. B. Pollack, M. E. Ockert, L. R. Doyle, and J. B. Dalton 1992. A photometric study of Saturn's F ring. *Icarus* **100**, 394–411.
- Shu, F. H., J. N. Cuzzi, and J. J. Lissauer 1983. Bending waves in Saturn's rings. *Icarus* **53**, 185–206.
- Sicardy, B., J. Lecacheux, P. Laques, R. Despia, and A. Auge 1982. Apparent thickness and scattering properties of Saturn's rings from March 1980 observations. *Astron. Astrophys.* **108**, 296–305.
- Throop, H. B., and L. W. Esposito 1998. G ring particle sizes derived from ring plane crossing observations. *Icarus* **131**, 152–166.
- Van de Hulst, H. C. 1974. The spherical albedo of a planet covered with a homogeneous cloud layer. *Astron. Astrophys.* **35**, 209–214.
- Westphal, J. A., W. A. Baum, A. P. Ingersoll, C. D. Barnet, E. M. De Jong, G. E. Danielson, and J. Caldwell 1992. Hubble Space Telescope observations of the 1990 equatorial disturbance on Saturn—Images, albedos, and limb darkening. *Icarus* **100**, 485–498.